

See discussions, stats, and author profiles for this publication at: <https://www.researchgate.net/publication/272391227>

# Surface-Assisted Reactions toward Formation of Graphene Nanoribbons on Au(110) Surface

ARTICLE *in* THE JOURNAL OF PHYSICAL CHEMISTRY C · JANUARY 2015

Impact Factor: 4.77 · DOI: 10.1021/jp509415r

---

CITATIONS

2

---

READS

74

## 13 AUTHORS, INCLUDING:



Emanuele Cavaliere

Catholic University of the Sacred Heart

31 PUBLICATIONS 192 CITATIONS

[SEE PROFILE](#)



Luca Gavioli

Catholic University of the Sacred Heart

76 PUBLICATIONS 767 CITATIONS

[SEE PROFILE](#)



Deborah Prezzi

Italian National Research Council

41 PUBLICATIONS 1,150 CITATIONS

[SEE PROFILE](#)



Elisa Molinari

Università degli Studi di Modena e Reggio Emilia

294 PUBLICATIONS 7,467 CITATIONS

[SEE PROFILE](#)

# Surface-Assisted Reactions toward Formation of Graphene Nanoribbons on Au(110) Surface

Lorenzo Massimi,<sup>\*,†</sup> Oualid Ourdjini,<sup>†</sup> Leif Lafferentz,<sup>‡</sup> Matthias Koch,<sup>‡</sup> Leonhard Grill,<sup>§,‡</sup> Emanuele Cavaliere,<sup>||</sup> Luca Gavioli,<sup>||</sup> Claudia Cardoso,<sup>⊥</sup> Deborah Prezzi,<sup>⊥</sup> Elisa Molinari,<sup>⊥,#</sup> Andrea Ferretti,<sup>\*,⊥</sup> Carlo Mariani,<sup>†</sup> and Maria Grazia Betti<sup>†</sup>

<sup>†</sup>Dipartimento di Fisica, Università di Roma La "Sapienza", 00185 Roma, Italy

<sup>‡</sup>Department of Physical Chemistry, Fritz-Haber-Institut der Max-Planck-Gesellschaft, 14195 Berlin, Germany

<sup>§</sup>Department of Physical Chemistry, University of Graz, 8010 Graz, Austria

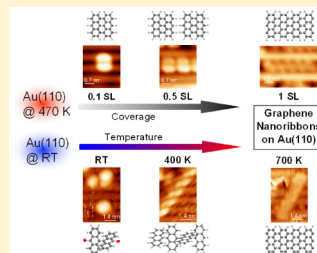
<sup>||</sup>i-LAMP & Dipartimento di Matematica e Fisica, Università Cattolica, 25121 Brescia, Italy

<sup>⊥</sup>Centro S3, CNR-Istituto Nanoscienze, 41125 Modena, Italy

<sup>#</sup>Dipartimento di Scienze Fisiche, Informatiche, Matematiche, Università di Modena e Reggio Emilia, 41125 Modena, Italy

## S Supporting Information

**ABSTRACT:** Scanning tunneling microscopy and X-ray spectroscopy measurements are combined to first-principles simulations to investigate the formation of graphene nanoribbons (GNRs) on Au(110), as based on the surface-mediated reaction of 10,10'-dibromo-9,9'-bianthracene (DBBA) molecules. At variance with Au(111), two different pathways are identified for the GNR self-assembly on Au(110), as controlled by both the adsorption temperature and the surface coverage of the DBBA molecular precursors. Room-temperature DBBA deposition on Au(110) leads to the same reaction steps obtained on Au(111), even though with lower activation temperatures. For DBBA deposition at 470 K, the cyclodehydrogenation of the precursors precedes their polymerization, and the GNR formation is fostered by increasing the surface coverage. While the initial stages of the reaction are found to crucially determine the final configuration and orientation of the GNRs, the molecular diffusion is found to limit in both cases the formation of high-density long-range ordered GNRs. Overall, the direct comparison between the Au(110) and Au(111) surfaces unveils the delicate interplay among the different factors driving the growth of GNRs.



## INTRODUCTION

Graphene—prototype of one-atom-thick two-dimensional material—attracts particular interest among  $\pi$ -based carbon nanostructures owing to its excellent transport properties,<sup>1</sup> though the intrinsic zero-energy gap reduces its impact for the design of nanodevices. Nanostructuring could help overcome these difficulties, since quantum confinement induces a band gap opening, as it was first observed on lithographically patterned graphene nanoribbons (GNRs).<sup>2,3</sup> However, ribbon widths smaller than 10 nm are needed to guarantee room temperature operation.<sup>4</sup>

An alternative route to lithography for the production of narrow GNRs relies on bottom-up approaches based on suitably designed molecular building blocks.<sup>5,6</sup> At variance with lithography, these methods have proven successful to reach GNR widths down to the subnanometer range and atomic control on the edges—both of them dictated by the molecular precursor—together with lengths from 20 nm<sup>5</sup> to 200 nm,<sup>6</sup> depending on the approach adopted. This has allowed to measure for the first time sizable band gaps larger than 2 eV and parabolic dispersion,<sup>7–9</sup> electric conductance,<sup>10</sup> and exciton-dominated optical response,<sup>11</sup> which are only a few

among the many intriguing properties predicted theoretically for these structures.<sup>4,12–15</sup>

One of the most promising bottom-up methods is based on the surface-mediated reaction of a specific class of oligomer precursors, like 10,10'-dibromo-9,9'-bianthracene<sup>5,16</sup> (DBBA, see Figure 1). Here the growth mechanism is catalyzed by the Au(111) metal surface, which favors the precursor dehalogenation;<sup>16</sup> polymerization and cyclodehydrogenation are then thermally activated by subsequent annealing steps at 470 and 670 K, respectively, leading to the formation of graphene-like ribbon assemblies.<sup>5</sup> Further studies monitoring the growth process by means of X-ray<sup>17,18</sup> and optical<sup>11</sup> spectroscopies have offered a better understanding of this mechanism, also by comparison with more reactive substrates than Au(111), like Cu(111).<sup>17</sup> In addition, it has been demonstrated that long-range ordering of GNRs can be achieved on the Au(788) vicinal surface, since the terrace anisotropy favors the synthesis of parallel GNRs.<sup>7,8</sup>

Received: September 17, 2014

Revised: December 20, 2014

Published: December 23, 2014

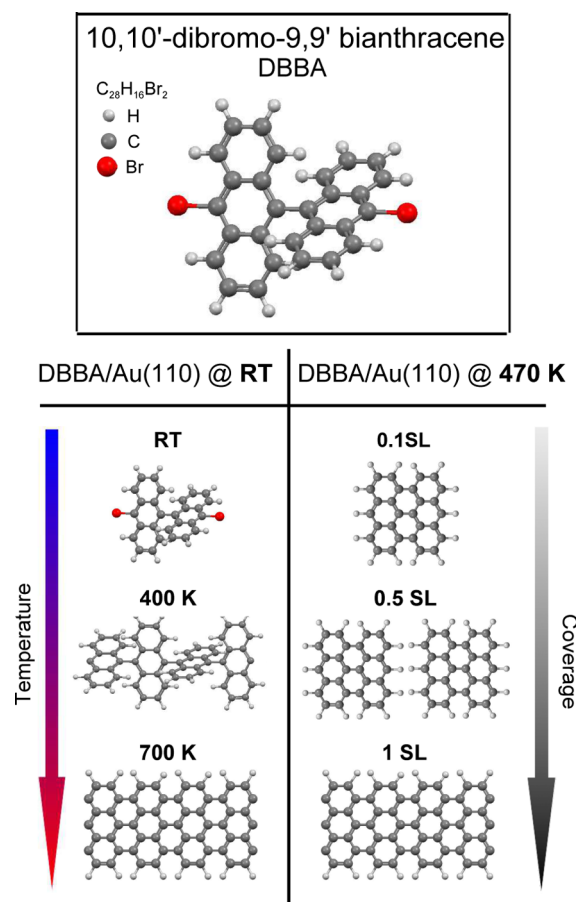


**Figure 1.** Ball-and-stick model of the 10,10'-dibromo-9,9'-bianthracene (DBBA) molecule (top panel); schematic representation of different reaction paths to the GNR formation after DBBA deposition on Au(110) at different substrate temperatures, i.e., room-temperature and 470 K, respectively (bottom panels).

Indeed, highly anisotropic surfaces, like vicinal or nano-patterned surfaces, can act as templates to drive the growth process along preferential directions. A naturally nanostructured gold template for long-range ordering of a variety of aromatic molecular species is the Au(110) surface, characterized by the minimum-energy  $1 \times 2$  reconstruction with 8.16 Å wide channels generated by missing rows along the  $[1\bar{1}0]$  direction.<sup>19</sup> The small energy differences between the Au  $1 \times 2$ ,  $1 \times 3$ ,  $1 \times 4$ , and  $1 \times 5$  reconstructions<sup>20</sup> tend to induce a malleable nature to the Au(110) surface, which can easily undergo further local reconstructions by forming ordered surface line defects, in turn enabling the allocation of molecular chains into long-range ordered structures.<sup>21–25</sup>

In this work, we explore different routes for the growth of GNRs on the Au(110) surface. We demonstrate that the DBBA adsorption temperature is a very crucial parameter on Au(110), since it determines when the dehalogenation and dehydrogenation processes take place and presents a strong interplay with the molecular mobility, at variance with the case of Au(111). Indeed, when the DBBA is deposited at room temperature (RT) and subsequently annealed at higher temperatures, the reaction pathway is the same as for Au(111), starting from the intact DBBA molecule and proceeding through polymerization and dehydrogenation toward the GNR formation.<sup>5</sup> On the contrary, adsorption at a higher temperature (470 K) causes a prompt dehalogenation and dehydrogenation, leading to flat

unpolymerized molecules due to the higher corrugation and interaction strength of Au(110) with respect to Au(111).

In order to fully understand the role of the different factors that drive or hinder the GNR formation, the growth processes have been investigated in depth by using a set of complementary experimental and theoretical techniques: scanning tunneling microscopy (STM) to determine the topography evolution; temperature-programmed X-ray photoelectron spectroscopy (TP-XPS) and near-edge X-ray absorption fine structure (NEXAFS) to control the chemical bonding during the GNR formation; ab initio density-functional theory (DFT) simulations for the investigation of the structural and stability properties of both polymer and GNR phases on the Au(110) substrate. Complex architectures, including GNRs parallel to the reconstructed chains or crossing the Au rows, are observed for the Au(110) surface depending on the growth parameters. The comparison with Au(111) highlights the role of surface corrugation, molecular diffusion and mobility, and molecule–substrate interaction, indicating that the initial state of the molecular precursors crucially determines the final configuration of GNRs on Au(110).

## METHODS

**Experimental Methods.** The STM experiments have been performed in two different ultrahigh-vacuum (UHV) chambers, all equipped with ancillary systems for sample cleaning, molecule deposition, and surface quality control. The STM instrument located at the Interdisciplinary Laboratories for Advanced Materials Physics (i-LAMP) of the Department of Mathematics and Physics at the Università Cattolica del Sacro Cuore (Brescia, Italy) is an OMICRON STM system. The tungsten tip has been prepared by chemical etching method in a 2 N NaOH solution and subsequently bombarded in UHV with high-energy electrons up to 1 keV, in order to eliminate residual tip contamination. Measurements have been carried out at room temperature. The second STM apparatus is a modified commercial low temperature Createc, at the Department of Physical Chemistry of the Fritz-Haber-Institut der Max-Planck-Gesellschaft (Berlin, Germany). Measurements have been carried out at about 10 K in constant-current mode. Bias voltages are given with respect to the sample (with the tip being grounded). The STM scale has been calibrated on the clean Au(110)- $1 \times 2$  surface.

Synchrotron-radiation XPS experiments have been performed at the SuperESCA beamline of the ELETTRA synchrotron radiation facility (Trieste, Italy).<sup>26</sup> A photon energy of 400 eV was used for both Br-3d and the C-1s core levels. Photoelectrons were collected at normal emission, with a Phoibos 150 mm hemispherical electron energy analyzer equipped with a homemade delay line detection system. Photoemission data have been normalized to the beam intensity, and the binding energy (BE) scale was calibrated using the Fermi edge of the Au substrate. Temperature-programmed XPS (TP-XPS) measurements were taken after deposition of about one monolayer of DBBA at liquid nitrogen temperature (80 K) in order to prevent any surface induced chemical reaction. Afterward, the sample temperature has been increased with a linear rate of 0.2 K/s, following *in situ* and in real-time by XPS the desorption process. With this procedure, by analyzing the Br-3d and the C-1s core-level intensity, binding energy, and line shape, we followed the temperature evolution of the molecular layer adsorbed on the substrate.

NEXAFS measurements across the C K-edge were taken at the SuperESCA beamline in the Auger yield detection mode, with linearly polarized radiation, with the electric field vector either parallel ( $\theta = 0^\circ$ , transverse electric field) or almost normal ( $\theta = 70^\circ$ , transverse magnetic field) to the surface plane, by rotating the sample, with  $\theta$  defined as the angle between the direction of the incident radiation and the surface normal. All the absorption spectra have been normalized to the beam intensity  $I_0$  measured at the same time by a gold mesh inserted in the optical path.

The base pressure in the ultrahigh-vacuum chambers of all the experimental stations was in the low  $10^{-10}$  mbar range. The Au(110) and Au(111) surfaces were cleaned by cycles of sputtering followed by annealing (800 eV Ar<sup>+</sup>, 820 K, subsequently 400 eV Ar<sup>+</sup>, 570 K). Sample cleanliness and long-range order were checked by means of XPS and low energy electron diffraction (LEED), respectively. The commercially purchased DBBA molecules (Richest Group Ltd.) were cleaned in UHV by repeated cycles of annealing close to the sublimation temperature. They were sublimated in UHV by means of homemade resistively heated quartz crucibles at a temperature of about 420 K, as measured by a thermocouple attached to the quartz crucible, in order to ensure the sublimation of intact molecules and to guarantee the reliability of the sublimation procedure in the different experimental chambers. The nominal single-layer (SL) coverage has been assumed as a compact monolayer of adsorbed molecules. The completion of a single layer has been determined by the stabilization of the  $1 \times 4$  Au(110) reconstruction, when the molecules are deposited at 470 K. The overall pressure during deposition was in the  $10^{-9}$  mbar range.

**Computational Details.** Density-functional theory (DFT) simulations were performed within the local density approximation (LDA) for the exchange-correlation potential, using a plane-wave basis set and ultrasoft pseudopotentials, as implemented in the Quantum-ESPRESSO package.<sup>27</sup> While more accurate functionals exist, including van der Waals corrected ones, we have chosen LDA for its better description of the Au lattice parameter (see Table S1 in the Supporting Information). We consider  $1 \times 2$ ,  $1 \times 3$ , and  $1 \times 4$  Au(110) surface reconstructions, both clean and with adsorbed polyanthryl and GNR. Graphene and GNR adsorbed on Au(111) were also investigated for comparison. An overview of all the different configurations considered here is reported in Figure 4.

The surfaces were modeled using a 9-layer (8-layer) slab of Au(110) for the  $1 \times 2$  and  $1 \times 4$  ( $1 \times 3$ ) reconstructions; symmetric slabs were chosen in order to avoid unphysical dipole moments across the system. For the  $1 \times 2$  and the  $1 \times 4$  ( $1 \times 3$ ) reconstructions an orthogonal  $4 \times 3\sqrt{2}$  ( $3 \times 3\sqrt{2}$ ) surface cell of Au(110) was employed in order to accommodate two primitive cells of the GNR. A top view of the units cells used in the calculations is shown in Figure 2. The in-plane lattice parameter was set to the LDA optimized parameter of bulk Au (4.05 Å). The atomic positions within the cell were fully optimized with a force threshold of 0.013 eV/Å. With this choice for the lattice parameter, the GNR presents a residual 1% stretching along the main axis, as compared to its free-standing optimized geometry. The kinetic energy cutoff for the wave functions (charge density) was set to 25 (300) Ry; the Brillouin zone was sampled by using a  $4 \times 8 \times 1$  ( $8 \times 8 \times 1$ ) k-points grid for the  $1 \times 2$  and the  $1 \times 4$  ( $1 \times 3$ ) reconstructions. Adsorption energies for both polymers and GNRs were

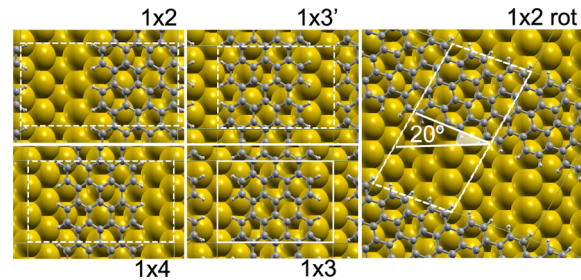


Figure 2. Top view of the unit cells used for the different surface reconstructions of the Au(110) surface.

computed as total energy differences with respect to the clean Au slab and the free-standing optimized geometry of the polymer/GNR. The convergence of the adsorption energy with layer thickness was checked for a 10-layer slab, showing differences lower than 1 meV/C atom. The relative stability of the different surface reconstructions is not taken into account in the evaluation of the adsorption energies since they are of the order of 1–2 meV/C (see Supporting Information).

## RESULTS AND DISCUSSION

**Growth and Structural Characterization. Room Temperature Deposition.** As a first approach to the growth of GNRs on the Au(110) surface, we deposited the DBBA molecules on Au(110) at room temperature (RT), followed by different annealing steps, in order to promote DBBA polymerization and subsequent cyclodehydrogenation upon thermal activation, as found on Au(111).<sup>5</sup> After each step of the growth process, that is, DBBA deposition at RT, first annealing step at 400 K (DBBA polymerization), and second annealing step at 700 K (cyclodehydrogenation and ribbon formation), the surface was imaged by STM. The STM images recorded at the different growth steps are shown in Figure 3. After the deposition of DBBA at a nominal coverage of 0.2 single layer (SL), the topographic image is characterized by bright protrusions on top of the  $1 \times 2$  Au reconstructed channels, which do not show any apparent ordering on the surface (Figure 3, left panel), which can be explained by the high molecular diffusion along the Au channels at RT. The STM profile shows an apparent height for the molecular protrusions of 5 Å; the lateral size and shape are consistent with adsorption of almost intact molecules, as confirmed by the spectroscopic measurements discussed later. The molecules are not completely flat due to the steric hindrance of their structure, characterized by repulsion among the inner hydrogen atoms of the two molecular lobes.

After annealing at 400 K the RT-deposited DBBA, the molecules assemble into a different structure: we observe chains characterized by alternate bright lobes with a periodicity of  $0.9 \pm 0.2$  nm, with a preferential orientation of about  $\pm(20 \pm 4)^\circ$  with respect to the Au [001] direction (Figure 3, central panel). However, from a statistical analysis of STM images, a 25% of polymer chains is also found aligned along the [110] direction and a smaller fraction few degrees off. The higher lobes of the chain show an apparent height of 2.5 Å with respect to the underlying Au rows. Comparing this value to that of the intact molecules (i.e.,  $\approx 5$  Å), a flattening of the molecular adsorption geometry is suggested. Nonetheless, the alternate-lobe pattern of the polyanthryl chains exhibits a less pronounced contrast than its counterpart on Au(111).<sup>5</sup> This can be attributed to the

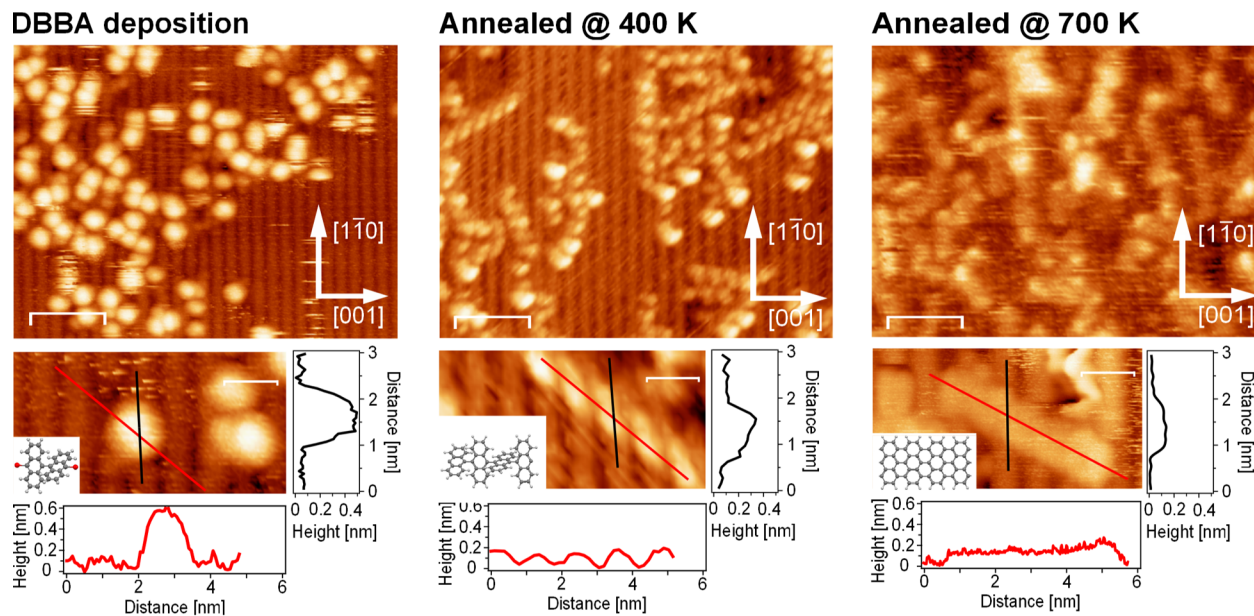


**Figure 3.** STM images at large and small scale of 0.2 SL DBBA adsorbed on Au(110) at RT (left panel), after annealing at 400 K (central panel), and after annealing at 700 K (right panel). Two different line profiles are shown for each structure: one along the gold chain direction (black line) and one along the longitudinal axis of the structures (red line). Images acquired at  $T = 300$  K in constant current mode. All STM images have been taken at the same bias voltage ( $-2$  V bias voltage,  $0.06$  nA tunneling current) in order to compare the evolution of apparent height. Scale bar of 4.8 and 1.4 nm for the large and small scale image, respectively.

flattening of the polymer upon adsorption on the corrugated surface.

Finally, we notice that this first annealing step following RT deposition does not give rise to a high density of long and ordered polymers, at variance with Au(111) or Cu(111) surfaces,<sup>5,17</sup> suggesting a lower molecular mobility on the corrugated Au(110). Even though the polyanthryl formation is activated after annealing at 400 K, the direct deposition on the hot substrate helps to improve the polymer growth.

Next, we further annealed the sample up to 700 K. The corresponding STM images are shown in the right panel of Figure 3. These images show that some polymer chains observed in the previous phase evolve into new structures characterized by a continuous charge density. The height profiles recorded along and across them show a constant height of  $1.5$  Å with respect to the Au rows, suggesting further flattening of the structure, in agreement with previous studies on Au(111).<sup>5,10</sup> Indeed, a higher annealing temperature is expected to induce the removal of inner hydrogen atoms and the formation of planar C–C bonded nanoribbons,<sup>5,17</sup> in perfect agreement with spectroscopic data presented in the following sections. The average GNRs length (about  $50$  Å) is shorter than the typical GNR length observed on Au(111) and Cu(111),<sup>5,17</sup> as a consequence of a reduced polymer length, with few of them maintaining the orientation of the original polymer chain.

In order to gain further insights into the growth process, we performed DFT simulations of the polyanthryl and GNR adsorbed on several Au(110) surface reconstructions. Inspired by the STM evidence described above, we have first considered two different adsorption configurations on the  $1 \times 2$  Au surface: (i) the GNR/polyanthryl aligned along the Au channels (i.e.,  $[1\bar{1}0]$  direction) and (ii) the GNR/polyanthryl rotated by  $20^\circ$  with respect to the direction perpendicular to the Au channels. While the first configuration is meant to mimic the isolated molecules on top of the Au rows, the second

one is observed as the preferential configuration for both the polymer and the ribbon phases. The optimized geometries and the computed adsorption energies are summarized in Figure 4. The remaining structures reported in this figure will be discussed in the following sections.

When the polyanthryl is aligned along the Au channels, the structure relaxes to a configuration where the system lies on top

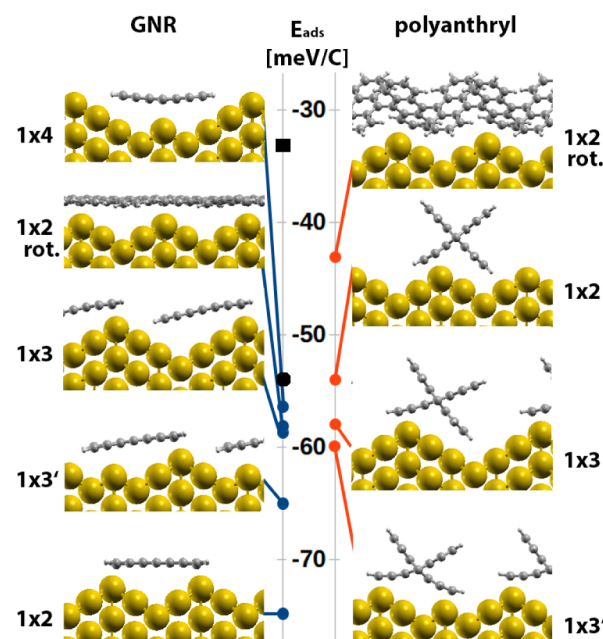


**Figure 4.** Calculated adsorption energies (meV/C atom) for the GNR (left panel) and polyanthryl (right panel) adsorbed onto the reconstructed  $1 \times 2$ ,  $1 \times 3$ , and  $1 \times 4$  Au (110) surfaces. The black dot (square) corresponds to the value computed for the GNR (graphene) adsorbed on the Au (111) surface.

of the Au row, as illustrated in Figure 4, irrespective of the initial configuration (i.e., on top of the Au rows or in the Au channels). The optimized geometry for the GNR lies instead within the Au channels. Concerning the second configuration, where the system crosses the Au channels, it can be seen that the only way to have the DBBA molecule commensurate with the surface is to rotate it, such that the two anthracene units (about 8.6 Å wide) can fit into the  $1 \times 2$  Au channels (8.1 Å wide), as illustrated in Figure 2.

When the DBBA molecules polymerize, the constraint of commensurability becomes even stronger and results in a tilting angle of about 20°, in perfect agreement with the experimental findings. Note that both configurations are asymmetric, with one of the anthracene units closer to the Au surface. In the configuration along (across) the channels, the minimum C–Au distances are 2.40 and 3.21 Å (2.34 and 3.09 Å) for the two units.

Figure 4 also reports the adsorption energies computed for each of the structures investigated here. For both the polyanthryl and the GNR on the  $1 \times 2$  surface we find that the configuration along the channels is more stable than the rotated configuration across the rows by 10–20 meV/C atom, at variance with experimental observations. This suggests that the growth of the GNR is not dominated by the stability of the GNR-surface interface but rather by the kinetics of the early stages of the process leading to the polymerization. In order to further investigate this issue, we simulated the dehalogenated precursor molecule on the  $1 \times 2$  surface, considering again the two orientations mentioned above (see Figure 5), i.e., with the

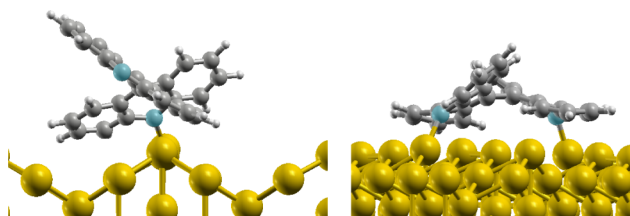


**Figure 5.** Optimized geometries computed within DFT for the debrominated DBBA. Left panel: molecule aligned along the Au rows, forming one bond with the surface. Right panel: the molecule rotated by 20° with respect to the direction perpendicular to the Au channels, showing the two bonds with the Au surface. The debrominated C atoms are in light blue.

molecule axis either parallel to the channels or rotated by about 20° with respect to the [001] direction. The resulting geometries are shown in Figure 5. The rotated conformation is 1.16 eV/molecule lower in energy than the aligned one. Indeed, the debrominated atoms of the rotated molecule can form two bonds with Au, with a rather flat conformation, while the aligned molecule only forms one C–Au bond, thus resulting less stable.

**High-Temperature Deposition.** In order to favor the molecule diffusion and possibly induce the formation of GNRs aligned along the Au channels, we have explored an alternative growth procedure, where the gold substrate is kept at a higher temperature (HT) of 470 K during deposition. A selected set of STM images, shown in Figure 6, reports the evolution from DBBA deposition to the GNR formation upon increasing coverage, without any further annealing step. At very low molecular density (0.1 SL), the isolated molecules appear as two bright and symmetric lobes bridging two adjacent Au

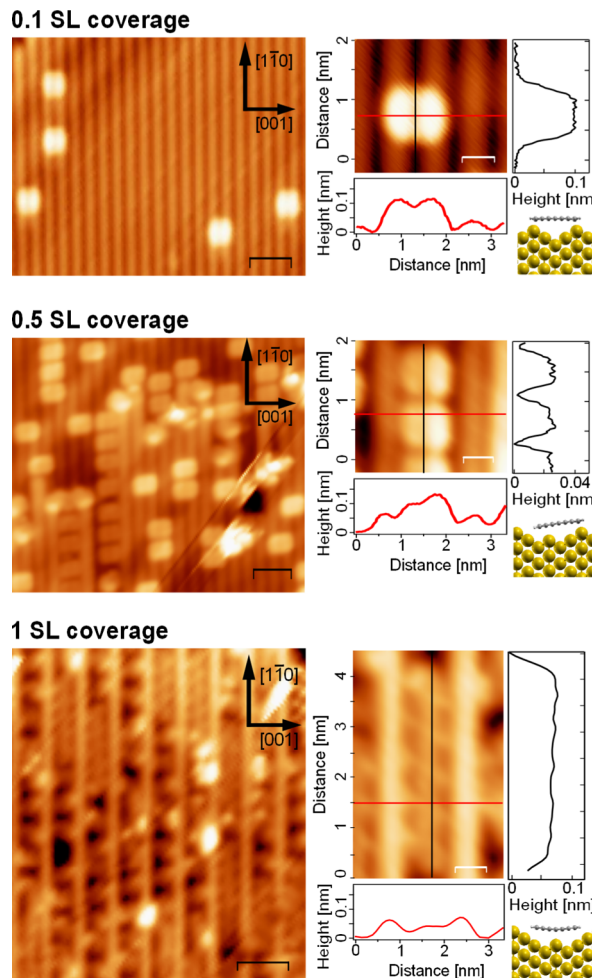


**Figure 6.** STM topography images at about 0.1 SL (upper panel), 0.5 SL (middle panel), and 1 SL (lower panel) of DBBA deposited on Au(110) maintained at 470 K temperature. Experimental profiles along the high symmetry directions of the substrate are reported in black and red lines on the small scale images. Side views of the Au cell and adsorbed molecule, as determined by theoretical calculations, are plotted close to the experimental line profiles. At 0.1 SL, a few isolated molecules are visible on top of the gold chains in the Au(110)- $1 \times 2$  reconstruction; at 0.5 SL, tilted molecular chains start to appear inside  $1 \times 3$ -reconstructed gold channels; at 1 SL, the molecular chains appear flatter and laying into  $1 \times 4$ -reconstructed gold channels. Images acquired at  $T = 10$  K (0.6 V bias voltage, 0.1 nA tunneling current). Scale bar of 2.4 and 0.7 nm for the large and small scale image, respectively.

rows suggesting a flat-lying structure. This is corroborated by the symmetrical lobe shape of the molecules, which recalls the calculated frontier orbital for gas-phase DBBA of a flat bisanthrene (bisanthene) molecule (see Supporting Information). Comparison with previous STM simulated images for the termini of the same GNRs on Au(111)<sup>28</sup> and with our own calculations of the molecular orbitals suggests that the molecules are also dehalogenated. Thus, the structural shape of HT-deposited DBBA on the Au(110) surface suggests that both dehalogenation and dehydrogenation processes take place already at 470 K, before any polymerization, as confirmed by the following spectroscopy data. Note that for the Au(111) surface the dehydrogenation requires a considerably higher temperature (above 600 K, see following temperature-programmed XPS data), whereas the molecular shape at 470 K still presents

higher protrusions associated with H–H repulsion twisting the phenyl groups.<sup>5</sup>

By increasing the molecular coverage up to 0.5 SL, the flat bisanthene components start to form ordered chains along the [1̄10] direction, either bridging two adjacent rows of the pristine 1 × 2 Au reconstruction, as observed for the isolated molecules, or inside rearranged (1 × 3) gold channels, as shown in the middle panel of Figure 6. In the latter case, the two molecular lobes show different intensity that, together with the line profile, suggests a tilted adsorption geometry within the 1 × 3 reconstructed Au channels.

At completion of the first single layer, the Au surface further rearranges into a 4-fold symmetry (confirmed by the LEED pattern reported in the Supporting Information), with elongated nanostructures still aligned along the channels ([1̄10] direction). The STM images of these nanostructures present a continuous charge density embedded into the 4-fold reconstructed gold rows (see Figure 6, lower panel). The homogeneous appearance and the characteristic point to the formation of GNRs, as indeed confirmed by the following spectroscopy measurements. Isolated bright protrusions suggest the coexistence of dehalogenated and dehydrogenated single molecules with GNRs segments. Note that the nanostructures assembled on top of the gold rows observed at low coverage are absent over all the investigated surface.

To complete our analysis, we simulated both polyanthryl and GNR adsorbed on 1 × 2, 1 × 3, and 1 × 4 reconstructed Au(110) surfaces by means of DFT calculations, as suggested by STM results. For the 1 × 3 reconstruction we considered two different surfaces, labeled 1 × 3 and 1 × 3', the latter with an extra row of Au atoms at the center of the Au channels. The optimized geometries and the computed adsorption energies are summarized in Figure 4. If we admit that the DBBA precursors (before and after dehydrogenation) present the same trends for the adsorption energy as their extended counterparts (polyanthryl and GNR), our results indicate that the flat molecules (or the GNR) would preferentially bridge the 1 × 2 Au rows, in agreement with the experimental observations. For the case of the 1 × 3 reconstructions, the GNR is found to lie tilted, with one side on top of the highest Au atoms, and the other side within the channels, thereby supporting the interpretation given above for the STM intensity difference of the molecular lobes. Finally, we have also considered a 1 × 4 reconstructed surface, where the GNR is found to lie (slightly bent but flat) within the Au channels, again in excellent agreement with the experimental observations.

While the theoretical findings corroborate the experimental observations regarding the final adsorption configuration over each reconstruction, the energetics indicates that the GNRs should assemble on the 1 × 2, and not on the 1 × 4, as found experimentally, which is less favorable by about 20 meV/C atom. As for the RT-deposition route, the preferable configuration for the GNRs seems to be determined by other factors than the energetic stability of the molecule–surface system. In particular, we suggest that Br, adsorbing in a 4-fold symmetry on the substrate,<sup>29</sup> could help the stabilization of the 1 × 4 reconstruction. In fact, Br atoms are found to segregate from the DBBA molecules and directly adsorbed on the Au(110) surface at 470 K (see following core-level spectroscopy discussion), thereby favoring the GNR alignment into the (1 × 4) gold channels (see Supporting Information).

**Core-Level Spectroscopies.** In order to achieve a deeper insight into the chemical processes taking place after DBBA adsorption on Au(110), we have investigated the system by temperature-programmed XPS, focusing on both the Br-3d and C-1s core levels and by near-edge X-ray absorption fine structure at the C K-edge. The same analysis has been applied to both the low-temperature (LT) and HT depositions.

**Low-Temperature Deposition.** To ensure the adsorption of intact molecules, we have deposited a single layer of DBBA on Au(110) kept at liquid nitrogen temperature. The DBBA/Au(110) system has been progressively annealed up to 700 K, while a TP-XPS measurement has been performed. The results in the energy region of the Br-3d core levels is reported in Figure 7, while the temperature evolution of the C-1s line shape is shown in Figure 8.

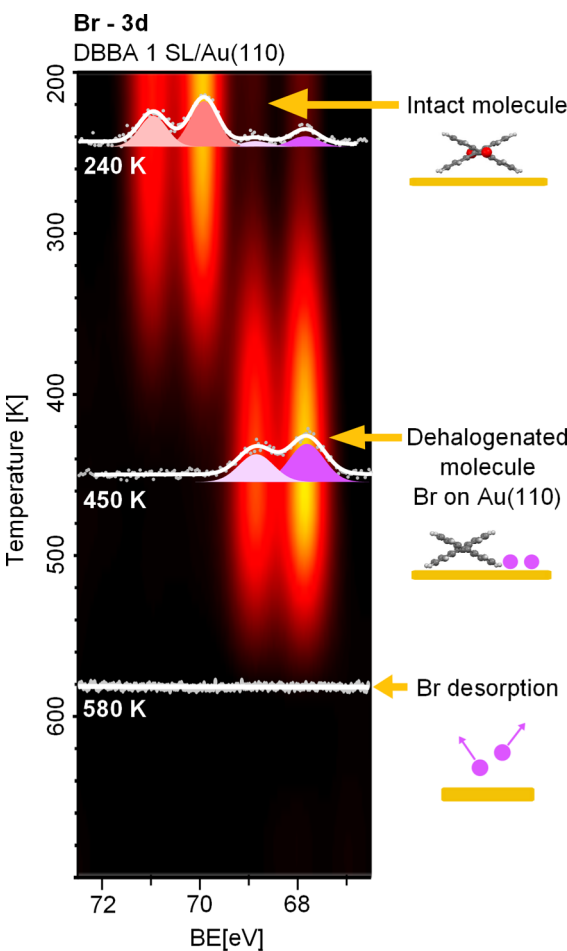


**Figure 7.** 2D map of the intensity of temperature-programmed XPS spectra at the Br-3d core levels for 1 SL of DBBA deposited on Au(110) at low temperature. A few Br-3d core levels spectra are plotted, selected at significant temperatures. Red peaks are assigned to Br atoms bonded to the molecule and purple peaks to isolated Br atoms adsorbed on the gold surface, as in the sketch shown in the right side of the figure.

The Br-3d core levels of the DBBA SL deposited on Au(110) at LT present the typical spin-orbit splitted lines, with the  $3d_{5/2}$  state at a binding energy of 69.9 eV. This value is 0.3 eV shifted with respect to the thick film (TF, not shown here) due to the interaction of the very first layer of DBBA molecules with Au(110). This is confirmed by the absence of a shift for DBBA

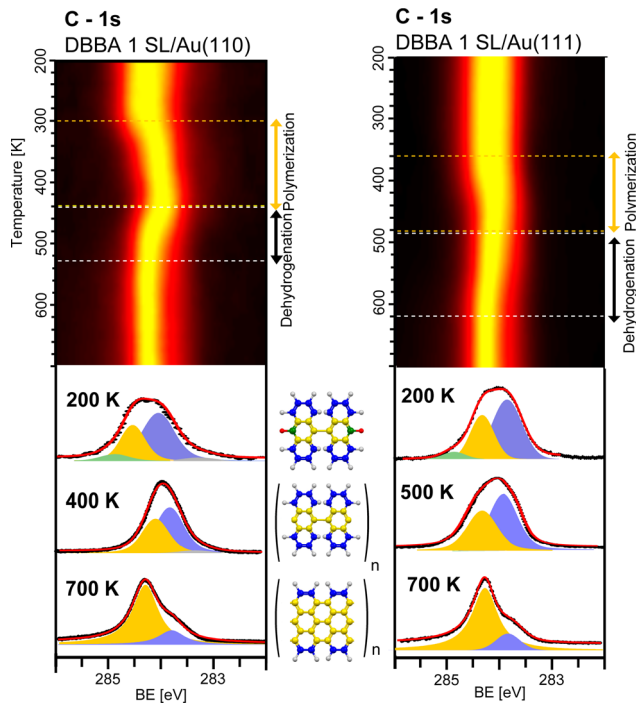


**Figure 8.** Evolution of the C-1s core level of DBBA deposited on Au(110) (left panel) and on Au(111) (right panel), as a function of temperature, reported as 2D color map. Selected spectra and fits for the initial, intermediate, and final phases of the molecular evolution are reported in the lower panels, sketched in the central panel with the following color legend: C–Br bond (green), C–H (blue), C–C (yellow), and C–metal (gray). Horizontal dashed lines mark the temperature limits for the polymerization phase as determined by the Br-3d core-level evolution and of dehydrogenation reaction as estimated from the C-1s line shape evolution.

on Au(111), where the interaction is expected to be weaker. The Br- $3d_{5/2}$  BE is consistent with bromine atoms covalently bonded to C<sup>30,31</sup> and to aromatic hydrocarbons,<sup>17,32</sup> confirming the adsorption of intact molecules. At RT, the intensity lowering of the Br component associated with the intact molecule reveals the beginning of the dehalogenation reaction. At the same time, a lower energy doublet appears (Br- $3d_{5/2}$  at 67.8 eV BE), which can be attributed to bare Br atoms adsorbed on the gold surface taking charge from the metal.<sup>33</sup> By following the intensity variation as a function of temperature, we find the maximum dehalogenation rate at 360 K and that the molecules are fully dehalogenated at 450 K. Further increasing the temperature, we find that the isolated Br atoms fully desorb from the Au(110) surface at 580 K.

Comparing these results on Au(110) with the Br-3d core levels for the DBBA SL adsorbed on Au(111) (reported in the Supporting Information), we observe no consistent change in Br-3d intensity or line shape up to 360 K, when dehalogenation starts; the maximum dehalogenation rate is found at 410 K, and total dehalogenation is achieved at 480 K, in agreement with the literature.<sup>17,32,34</sup> Therefore, the DBBA dehalogenation takes place at lower temperature on Au(110) than on the closed-packed Au(111), revealing a catalytic role of the gold reconstruction in the polymerization reaction. Indeed, surface defects are known to play an important role in catalysis,<sup>35,36</sup> and the reconstructed Au atomic rows can be at the origin of a stronger molecule–substrate interaction, acting as preferential

sites for the debromination reaction, as reported for other dehalogenative polymerization reactions on stepped surfaces.<sup>37</sup>

We next move to the analysis of the evolution of the C-1s line shape for DBBA as a function of the annealing temperature on both Au(110) and Au(111), as shown in Figure 8. The C-1s core levels for the intact DBBA molecule on both surfaces present three main components related to C–H (blue), C–C (yellow), and C–Br (green) bonds, as deduced by fitting the data with Voigt functions. For DBBA/Au(110) (Figure 8, left panel), we observe three main components at 284.6, 284.1, and 284.3 eV of BE, assigned to C–C, C–H, and C–Br bonds, respectively. The fitting curves give intensity ratios of the different C components in agreement, within about 5%, with those expected on the basis of the DBBA stoichiometry (C–H:C–C:C–Br = 16:10:2), thus confirming the adsorption of intact molecules (see Supporting Information). In the case of Au(111) (Figure 8, right panel), the three C-1s components of DBBA deposited at LT are found at 284.3, 283.8, and 284.7 eV BEs, in very good agreement with a very recent experiment for DBBA deposited on Au(111) at RT<sup>17</sup> and with attributions for other aromatic molecules adsorbed on noble metal substrates.<sup>32,34,35,38–40</sup> The shift of 0.3 eV toward higher BE for the C-1s line shape of DBBA on Au(110) with respect to Au(111) can be assigned to the stronger interaction with the substrate, in agreement with a similar shift observed on high interactive Cu(111).<sup>17</sup>

At variance with DBBA/Au(111), a further low-intensity and broad C-1s component at lower BE must be considered to fit the spectra of DBBA/Au(110). According to the literature, this low-BE component is characteristic of radical C atoms interacting with the underlying metal surface.<sup>17,32</sup> Thus, it could originate from a direct C(radical)–Au interaction from unsaturated adsorbates. Its presence is a clear signature of an interaction of the molecules with the Au(110) substrate, as already observed for other molecular species,<sup>41,42</sup> confirming the higher interaction exerted by the Au(110) corrugated surface with respect to Au(111), where this peak is absent. Despite the presence of this low-BE component, we note that the dominant phase at this temperature is represented by intact DBBA molecules.

Upon progressively annealing the DBBA SL on both Au surfaces up to 700 K, the C-1s line shape narrows, and different phases can be identified. First, the C–Br component disappears as a result of the Br removal from the molecule, while the other components display a shift of a few tenths of an electronvolt toward lower BEs, larger on Au(110) than on Au(111) (see Table 1 in the Supporting Information). This initial phase is associated with the formation of the polyanthryl precursor,<sup>5</sup> which starts at about 320 and 360 K on Au(110) and Au(111), respectively, in agreement with the results on the evolution of Br-3d core levels discussed above.

In a second temperature range, the C-1s core level slightly shifts to higher binding energies on both surface due to the beginning of the cyclodehydrogenation reaction with expected formation of GNR on Au(111).<sup>5,17</sup> Above 570 K (620 K), the C-1s position and line shape on Au(110) [Au(111)] remain unchanged up to 700 K, showing only two components: the major C–C component, associated with the formation of GNRs, and a less intense C–H component, due to residual H at the GNR edges. We notice that the best fit for the C–C graphene component is obtained by using a Doniach–Sunjic line shape.<sup>43</sup> The binding energy of the components is the same on the two substrates, with C–C bond at 284.3 eV and C–H at

283.8 eV (the latter in agreement with hydrogenated graphene on Au),<sup>44</sup> and the ratio of the C–C and C–H components reflects the stoichiometry expected for GNRs decorated with edge hydrogen atoms. The observation of the same line shape on Au(110) and Au(111) demonstrates the formation of the same phase on both substrates at 700 K, proving the synthesis of GNRs also on Au(110). Finally, we note that this reaction proceeds with a wider temperature range ( $\Delta T = 150$  K) on Au(111) than on Au(110) ( $\Delta T = 90$  K), which we attribute to the different interaction of the polymer precursor with the two substrates.

In order to further confirm the formation of GNRs on Au(110), we performed NEXAFS measurements at the C K-edge. Figure 9 shows a selected set of C K-edge NEXAFS

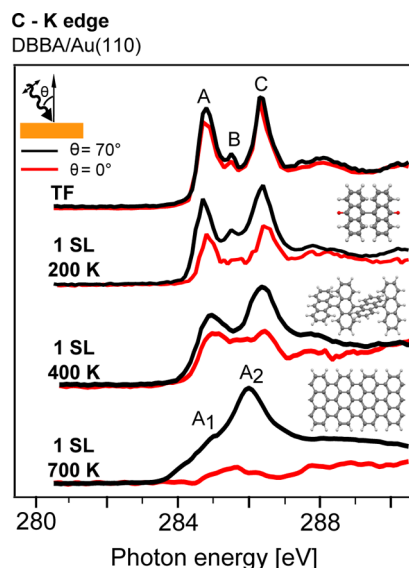


**Figure 9.** C K-edge linearly polarized NEXAFS spectra for a thin film (topmost data) and of a single layer of DBBA deposited on Au(110) at low temperature, after subsequent annealing temperature steps. Normal incidence ( $\theta = 0^\circ$ ) spectra (red lines) and quasi-grazing incidence ( $\theta = 70^\circ$ ) spectra (black lines).

spectra obtained either from a DBBA-TF or from a DBBA-SL grown on the Au(110) substrate upon increasing annealing temperatures. NEXAFS spectra of both SL and TF present distinct absorption features in the 284–288 eV photon energy region, assigned to transitions from the C-1s to the  $\pi^*$  resonances, and broader structures at higher photon energy, associated with  $\sigma^*$  orbitals, which are consistent with previous experimental and theoretical results on the absorption spectra of  $\pi$ -conjugated molecules adsorbed on noble metal surfaces.<sup>17,18,35,45–48</sup>

In the DBBA thick film, where the absence of dichroism indicates the formation of a solid disordered molecular phase, the first three main resonances are located at 284.3 eV (A peak), 285 eV (B peak), and 285.9 eV (C peak) of photon energy. The A and C manifold peaks can be assigned to transitions from the C-1s state to the first two lower unoccupied molecular orbitals (LUMO and LUMO +1).<sup>45,49–51</sup> In linear aromatic polymers, the LUMO is mainly localized on C atoms bonded to hydrogen, while the LUMO+1 is localized on C atoms bonded to C.<sup>45,51,52</sup> The B peak can be attributed instead to transition from the C-1s to a final state mainly localized on C–Br bonds. Much broader features in the

292–310 eV photon energy range (not shown in the figure) can be finally associated with transitions into the continuum of states related to molecular orbitals mainly involving the C–C bonds.

The line shape of the C K-edge NEXAFS data of the DBBA SL at LT very much resembles that of the TF, revealing adsorption of intact molecules, in agreement with the previous discussion on core levels, as also very recently observed for the adsorption of DBBA on Au(111).<sup>17</sup> Looking at the intensity dependence of these  $\pi^*$  resonances as a function of the incident polarized photons, we observe a reduction using in-plane polarized light, which can be due to non-completely-flat molecular orientation at the SL stage, as expected by steric hindrance of facing hydrogen atoms.<sup>53,54</sup>

After annealing the sample at 400 K, the resonance B (related to C–Br bonds) is quenched, in agreement with the XPS data regarding the precursor debromination and with the formation of polyanthryl precursors in STM images. The NEXAFS signal start to show a slight dichroism, in agreement with a molecular arrangement of the polyanthryl precursors oriented with different angles with respect to the surface plane.<sup>5,54</sup> The absorption spectra appear very similar to those of the anthracene C K-edge<sup>45</sup> due to the geometrical arrangement of the polyanthryl precursor, which can be described as formed by adjacent anthracene monomers connected by C–C bonds. Furthermore, the resonance A (C-1s  $\rightarrow$  LUMO) presents an intensity reduction and broadening as a direct consequence of the polymer–Au interaction. This reduction could be attributed to a partial filling of the LUMO by charge transfer from the underlying metallic states and to a symmetry reduction resulting from a polymer distortion on the corrugated gold surface. The C K-edge absorption spectra of polyanthryl on Au(111) does not show the same intensity reduction of the C resonance related to the C–H bonding due to lower interaction of the polymer with the substrate (Supporting Information and ref 17).

After annealing at 700 K, a dramatic change in the line shape of the C K-edge occurs, and two novel features are observed, A<sub>1</sub> and A<sub>2</sub>, both assigned to  $\pi^*$  resonances in view of the strong linear dichroism. The A<sub>1</sub> resonance is related to a decrease of the previous A resonance, due to the reduction of hydrogen amount following the formation of GNRs. A similar line shape of the C K-edge has been also observed in low-interacting graphene on Ir(111)<sup>55</sup> and in very large aromatic molecules planarly adsorbed on surfaces,<sup>56</sup> though with a broader line shape. This broadening can be attributed to the coexistence of inequivalent C atoms in the graphene nanostructures (C atoms in the honeycomb network and at the edges) and to nanoribbons with different length and size. The spectroscopic similarity of the C K-edge and C-1s core-level for the C-nanostructures assembled on both Au(111) and Au(110) gives a further proof of the polymerization and subsequent formation of GNRs on Au(110).

**High-Temperature Deposition.** Concerning the high-temperature deposition phase, spectroscopic signatures of the formation of carbon nanostructures can be obtained by comparing the XPS C-1s core levels and the C K-edge absorption data acquired on the Au(110) surface after adsorption of the molecules at 470 K, with those of the Au(111) surface after annealing at 700 K, following the procedure established in ref 5.

The C-1s line shape is characterized for both systems by a main peak localized at about 284.3 eV of binding energy and a

shoulder at 283.7 eV BE, as reported in Figure 10 (upper panel). For both systems the main peak, assigned to C–C

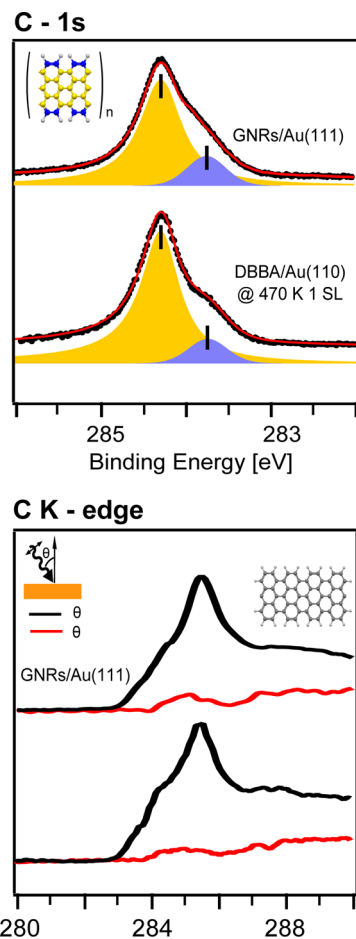


**Figure 10.** XPS C 1s (top panel) and NEXAFS C K-edge (bottom panel) are reported for the phase shown in the bottom panel of Figure 6 with comparison with the line shape of GNRs obtained on Au(111) obtained by procedure described in ref 5.

bonds, is dominant, with a residual signal from C–H contribution at lower BE, which is also present when depositing DBBA at room temperature, as discussed in the previous paragraphs. The BE and line shape of the C-1s signal for both systems are typical of formation of GNRs on Au.<sup>17</sup> Strong similarities between GNRs formed on Au(110) and on Au(111) can also be detected at the carbon K-edge, as shown in Figure 10 (lower panel). In particular, for the out-of-plane ( $\theta = 70^\circ$ ) polarization, the main  $\pi^*$  resonance and the residual C–H bump at lower photon energy for the GNR on Au(110) are peaked at the same photon energies observed also for GNRs on Au(111).<sup>17</sup> The line shape reveals the formation of H-terminated graphene nanoribbons for both systems. The dichroic signal (out-of-plane vs in-plane polarization) of GNRs on Au(110) confirms their flat configuration, when they are embedded into the Au reconstructed channels, in agreement with the presence of isolated GNRs observed by STM.

The lower molecular mobility expected on this naturally corrugated surface (either for molecules on-top of the  $1 \times 2$  reconstruction or inside the  $1 \times 4$  channels), whose potential barrier hinders the formation of ordered chains, prevent formation of a high density of GNR, in contrast with the Au(111) or Cu(111) flat surfaces.<sup>5,17</sup> When the molecules are

deposited at 470 K with single layer coverage, they lay mainly inside the channels of the  $1 \times 4$  Au reconstruction. This means that the reaction can take place only along the gold channels and is further limited by the fact that the molecules are already dehalogenated and dehydrogenated. This leads to the simultaneous presence of short segments of GNRs aligned along the Au rows. These segments are originated by molecules that follow the usual path. Since both reactions take place simultaneously, the molecular diffusion is hindered and the GNRs length strongly reduced. On the other hand, when the molecules are deposited at RT, they are intact but forced to diffuse only along the  $[1\bar{1}0]$  direction, giving rise to the features well described in the previous section.

## CONCLUSIONS

To conclude, we have presented a detailed investigation of the chemical processes leading to the GNR formation on Au(110), after DBBA adsorption. Our study combines STM topographic information to core-level X-ray spectroscopy data recorded during the synthesis, thus providing real-time fingerprints of the reaction on different gold surfaces. Experimental data have been complemented and further interpreted on the basis of ab initio DFT simulations.

We have explored two thermally activated synthetic routes by depositing DBBA either at RT or at 470 K. In the first case, we find a picture similar to that observed on Au(111), but with lower thermal offsets for the different reaction steps. In the latter, the precursor dehydrogenation is found to take place before polymerization, and the GNR formation is obtained through the coalescence of flattened molecules at increasing the surface coverage. The final orientation of the GNRs is also found to depend on the growth parameters, with carbon nanostructures either aligned or  $70^\circ$  tilted with respect to the gold chain reconstruction.

The comparison with the flatter and less interacting Au(111) surface shows that the GNR synthesis derives from a fine interplay among the molecular diffusion, the surface roughness, and the molecule–surface interaction. Here, the molecule diffusion rather than the molecule–surface interaction plays a pivotal role in the GNR growth: while long GNRs can be formed even on highly interacting surfaces, like Cu(111),<sup>17</sup> our findings identify the low molecular mobility due to the Au(110) corrugation as the main factor limiting GNR length and density.

## ASSOCIATED CONTENT

### S Supporting Information

Au lattice parameters computed within several functionals and reconstruction energies differences for several Au (110) surfaces; the calculation of the frontier lowest unoccupied molecular orbital (LUMO) for the flattened DBBA molecule (bisanthene) in gas phase, with and without the Br end atoms; the XPS analysis of the Br-3p core levels in the different phases of DBBA molecular adsorption on Au(110); the C-1s core level fitting parameters; the  $1 \times 4$  Au(110) reconstruction by STM and LEED as produced by Br adsorption; a full set of TP-XPS and NEXAFS data for DBBA deposited on Au(111), for comparison with the present data on Au(110). This material is available free of charge via the Internet at <http://pubs.acs.org>.

## AUTHOR INFORMATION

### Corresponding Authors

\*E-mail lorenzo.massimi@uniroma1.it (L.M.).

\*E-mail andrea.ferretti@nano.cnr.it (A.F.).

**Notes**

The authors declare no competing financial interest.

**ACKNOWLEDGMENTS**

We are grateful to the staff members of the SuperEsca beamline at the Elettra synchrotron radiation facility (Trieste, Italy) for their kind support. This work was funded by MIUR PRIN Grant No. 20105ZZTSE "GRAF", by Sapienza University funds, and by the Elettra Sincrotrone Trieste support for users. We acknowledge partial support from MIUR through grants FIRB-RBFR08FOAL (A.F. and C.C.) and FIRB-RBFR12SWOJ (D.P.) and from MAE (US14GR12). We also acknowledge the European Project AtMol for supporting the STM measurements in Berlin and the PRACE project for providing computer time on FERMI at CINECA (Grant No. PRA06\_1348).

**REFERENCES**

- (1) Neto, A. C.; Guinea, F.; Peres, N.; Novoselov, K. S.; Geim, A. K. The Electronic Properties of Graphene. *Rev. Mod. Phys.* **2009**, *81*, 109.
- (2) Han, M. Y.; Özyilmaz, B.; Zhang, Y.; Kim, P. Energy Band-Gap Engineering of Graphene Nanoribbons. *Phys. Rev. Lett.* **2007**, *98*, 206805.
- (3) Chen, Z.; Lin, Y.-M.; Rooks, M. J.; Avouris, P. Graphene Nano-Ribbon Electronics. *Physica E* **2007**, *40*, 228–232.
- (4) Nakada, K.; Fujita, M.; Dresselhaus, G.; Dresselhaus, M. S. Edge State in Graphene Ribbons: Nanometer Size Effect and Edge Shape Dependence. *Phys. Rev. B* **1996**, *54*, 17954.
- (5) Cai, J.; Ruffieux, P.; Jafaar, R.; Bieri, M.; Braun, T.; Blankenburg, S.; Muoth, M.; Seitsonen, A. P.; Saleh, M.; Feng, X.; et al. Atomically Precise Bottom-up Fabrication of Graphene Nanoribbons. *Nature (London)* **2010**, *466*, 470–473.
- (6) Narita, A.; Feng, X.; Hernandez, Y.; Jensen, S. A.; Bonn, M.; Yang, H.; Verzhbitskiy, I. A.; Casiraghi, C.; Hansen, M. R.; Koch, A. H. R.; et al. Synthesis of Structurally Well-Defined and Liquid-Phase-Processable Graphene Nanoribbons. *Nat. Chem.* **2014**, *6*, 126–132.
- (7) Ruffieux, P.; Cai, J.; Plumb, N. C.; Patthey, L.; Prezzi, D.; Ferretti, A.; Molinari, E.; Feng, X.; Müllen, K.; Pignedoli, C. A.; et al. Electronic Structure of Atomically Precise Graphene Nanoribbons. *ACS Nano* **2012**, *6*, 6930–6935.
- (8) Linden, S.; Zhong, D.; Timmer, A.; Aghdassi, N.; Franke, J. H.; Zhang, H.; Feng, X.; Müllen, K.; Fuchs, H.; Chi, L.; et al. Electronic Structure of Spatially Aligned Graphene Nanoribbons on Au (788). *Phys. Rev. Lett.* **2012**, *108*, 216801.
- (9) Chen, Y.-C.; de Oteyza, D. G.; Pedramrazi, Z.; Chen, C.; Fischer, F. R.; Crommie, M. F. Tuning the Band Gap of Graphene Nanoribbons Synthesized from Molecular Precursors. *ACS Nano* **2013**, *7*, 6123–6128.
- (10) Koch, M.; Ample, F.; Joachim, C.; Grill, L. Voltage-Dependent Conductance of a Single Graphene Nanoribbon. *Nat. Nanotechnol.* **2012**, *7*, 713–717.
- (11) Denk, R.; Hohage, M.; Zeppenfeld, P.; Cai, J.; Pignedoli, C. A.; Söde, H.; Fasel, R.; Feng, X.; Klaus, M.; Wang, S.; et al. Exciton-Dominated Optical Response of Ultra-Narrow Graphene Nanoribbons. *Nat. Commun.* **2014**, *5*, 4253.
- (12) Son, Y.-W.; Cohen, M. L.; Louie, S. G. Energy Gaps in Graphene Nanoribbons. *Phys. Rev. Lett.* **2006**, *97*, 216803.
- (13) Prezzi, D.; Varsano, D.; Ruini, A.; Marini, A.; Molinari, E. Optical Properties of Graphene Nanoribbons: The Role of Many-Body Effects. *Phys. Rev. B* **2008**, *77*, 041404.
- (14) Prezzi, D.; Varsano, D.; Ruini, A.; Molinari, E. Quantum Dot States and Optical Excitations of Edge-Modulated Graphene Nanoribbons. *Phys. Rev. B* **2011**, *84*, 041401.
- (15) Yazyev, O. V. A Guide to the Design of Electronic Properties of Graphene Nanoribbons. *Acc. Chem. Res.* **2013**, *46*, 2319–2328.
- (16) Grill, L.; Dyer, M.; Lafferentz, L.; Persson, M.; Peters, M. V.; Hecht, S. Nano-Architectures by Covalent Assembly of Molecular Building Blocks. *Nat. Nanotechnol.* **2007**, *2*, 687–691.
- (17) Simonov, K. A.; Vinogradov, N. A.; Vinogradov, A. S.; Generalov, A. V.; Zagrebina, E. M.; Mårtensson, N.; Cafolla, A. A.; Carpy, T.; Cunniffe, J. P.; Preobrazenski, A. B. Effect of Substrate Chemistry on the Bottom-Up Fabrication of Graphene Nanoribbons: Combined Core-Level Spectroscopy and STM Study. *J. Phys. Chem. C* **2014**, *118*, 12532–12540.
- (18) Batra, A.; Cvetko, D.; Kladnik, G.; Adak, O.; Cardoso, C.; Ferretti, A.; Prezzi, D.; Molinari, E.; Morgante, A.; Venkataraman, L. Probing the Mechanism for Graphene Nanoribbon Formation on Gold Surfaces through X-Ray Spectroscopy. *Chem. Sci.* **2014**, *5*, 4419–4423.
- (19) Ercolelli, F.; Bartolini, A.; Garofalo, M.; Parrinello, M.; Tosatti, E. Molecular Dynamics Studies of Gold Surfaces. *Phys. Scr.* **1987**, *1987*, 399.
- (20) Garofalo, M.; Tosatti, E.; Ercolelli, F. Structure, Energetics, and Low-Temperature Behaviour of the Au (110) Reconstructed Surface. *Surf. Sci.* **1987**, *188*, 321–326.
- (21) Kühnle, A.; Molina, L.; Linderoth, T. R.; Hammer, B.; Besenbacher, F. Growth of Unidirectional Molecular Rows of Cysteine on Au (110)-(1×2) Driven by Adsorbate-Induced Surface Rearrangements. *Phys. Rev. Lett.* **2004**, *93*, 086101.
- (22) Evangelista, F.; Ruocco, A.; Pasca, D.; Baldacchini, C.; Betti, M. G.; Corradini, V.; Mariani, C. Au(110) Induced Reconstruction by π Conjugated Molecules Adsorption Investigated by Photoemission Spectroscopy and Low Energy Electron Diffraction. *Surf. Sci.* **2004**, *566*–568 (Part 1), 79–83.
- (23) Betti, M. G.; Gargiani, P.; Mariani, C.; Biagi, R.; Fujii, J.; Rossi, G.; Resta, A.; Fabris, S.; Fortuna, S.; Torrelles, X.; et al. Structural Phases of Ordered FePc-Nanochains Self-Assembled on Au(110). *Langmuir* **2012**, *28*, 13232–13240.
- (24) Fortuna, S.; Gargiani, P.; Betti, M. G.; Mariani, C.; Calzolari, A.; Modesti, S.; Fabris, S. Molecule-Driven Substrate Reconstruction in the Two-Dimensional Self-Organization of Fe-Phthalocyanines on Au (110). *J. Phys. Chem. C* **2012**, *116*, 6251–6258.
- (25) Bavdek, G.; Cossaro, A.; Cvetko, D.; Africh, C.; Blasetti, C.; Esch, F.; Morgante, A.; Floreano, L. Pentacene Nanorails on Au (110). *Langmuir* **2008**, *24*, 767–772.
- (26) Baraldi, A.; Comelli, G.; Lizzit, S.; Kiskinova, M.; Paolucci, G. Real-Time X-Ray Photoelectron Spectroscopy of Surface Reactions. *Surf. Sci. Rep.* **2003**, *49*, 169–224.
- (27) Giannozzi, P.; Baroni, S.; Bonini, N.; Calandra, M.; Car, R.; Cavazzoni, C.; Ceresoli, D.; Chiarotti, G. L.; Cococcioni, M.; Dabo, I.; et al. QUANTUM ESPRESSO: a Modular and Open-Source Software Project for Quantum Simulations of Materials. *J. Phys.: Condens. Matter* **2009**, *21*, 395502.
- (28) Talirz, L.; Söde, H.; Cai, J.; Ruffieux, P.; Blankenburg, S.; Jafaar, R.; Berger, R.; Feng, X.; Müllen, K.; Passerone, D.; et al. Termini of Bottom-Up Fabricated Graphene Nanoribbons. *J. Am. Chem. Soc.* **2013**, *135*, 2060–2063.
- (29) Zou, S.; Gao, X.; Weaver, M. J. Electrochemical Adsorbate-Induced Substrate Restructuring: Gold (110) in Aqueous Bromide Electrolytes. *Surf. Sci.* **2000**, *452*, 44–57.
- (30) Brieva, A.; Jäger, C.; Huisken, F.; Šiller, L.; Butenko, Y. V. A Sensible Route to Covalent Functionalization of Carbon Nanoparticles with Aromatic Compounds. *Carbon* **2009**, *47*, 2812–2820.
- (31) Palma, C.-A.; Diller, K.; Berger, R.; Welle, A.; Bjrk, J.; Cabellos, J. L.; Mowbray, D. J.; Papageorgiou, A. C.; Ivleva, N. P.; Matich, S.; et al. Photoinduced C - C Reactions on Insulators toward Photolithography of Graphene Nanoarchitectures. *J. Am. Chem. Soc.* **2014**, *136*, 4651–4658.
- (32) Gutzler, R.; Cardenas, L.; Lipton-Duffin, J.; El Garah, M.; Dinca, L. E.; Szakacs, C. E.; Fu, C.; Gallagher, M.; Vondracek, M.; Rybachuk, M.; et al. Ullmann-Type Coupling of Brominated Tetraphienoanthracene on Copper and Silver. *Nanoscale* **2014**, *6*, 2660–2668.
- (33) Pijpers, A.; Meier, R. J. Adhesion Behaviour of Polypropylenes after Flame Treatment Determined by XPS (ESCA) Spectral Analysis. *J. Electron Spectrosc. Relat. Phenom.* **2001**, *121*, 299–313.
- (34) Di Giovannantonio, M.; El Garah, M.; Lipton-Duffin, J.; Meunier, V.; Cardenas, L.; Fagot Revurat, Y.; Cossaro, A.; Verdini, A.;

- Perepichka, D. F.; Rosei, F.; et al. Insight into Organometallic Intermediate and Its Evolution to Covalent Bonding in Surface-Confining Ullmann Polymerization. *ACS Nano* **2013**, *7*, 8190–8198.
- (35) Lee, A. F.; Chang, Z.; Hackett, S. F.; Newman, A. D.; Wilson, K. Hydrodebromination of Bromobenzene over Pt (111). *J. Phys. Chem. C* **2007**, *111*, 10455–10460.
- (36) Meyer, R.; Lemire, C.; Shaikhutdinov, S. K.; Freund, H.-J. Surface Chemistry of Catalysis by Gold. *Gold Bull.* **2004**, *37*, 72–124.
- (37) Saywell, A.; Schwarz, J.; Hecht, S.; Grill, L. Polymerization on Stepped Surfaces: Alignment of Polymers and Identification of Catalytic Sites. *Angew. Chem., Int. Ed.* **2012**, *51*, 5096–5100.
- (38) von Schenck, H.; Weissenrieder, J.; Hellden, S.; Åkermark, B.; Göthelid, M. Reactions of Iodobenzene on Pd (1 1 1) and Pd (1 1 0). *Appl. Surf. Sci.* **2003**, *212*, 508–514.
- (39) Baldacchini, C.; Allegretti, F.; Gunnella, R.; Betti, M. G. Molecule–Metal Interaction of Pentacene on Copper Vicinal Surfaces. *Surf. Sci.* **2007**, *601*, 2603–2606.
- (40) Evangelista, F.; Ruocco, A.; Gotter, R.; Cossaro, A.; Floreano, L.; Morgante, A.; Crispoldi, F.; Betti, M. G.; Mariani, C. Electronic States of CuPc Chains on the Au(110) Surface. *J. Chem. Phys.* **2009**, *131*, 174710.
- (41) Massimi, L.; Angelucci, M.; Gargiani, P.; Betti, M. G.; Montoro, S.; Mariani, C. Metal-Phthalocyanine Ordered Layers on Au (110): Metal-Dependent Adsorption Energy. *J. Chem. Phys.* **2014**, *140*, 244704.
- (42) Betti, M. G.; Gargiani, P.; Frisenda, R.; Biagi, R.; Cossaro, A.; Verdini, A.; Floreano, L.; Mariani, C. Localized and Dispersive Electronic States at Ordered FePc and CoPc Chains on Au (110). *J. Phys. Chem. C* **2010**, *114*, 21638–21644.
- (43) Preobrajenski, A.; Ng, M. L.; Vinogradov, A.; Mårtensson, N. Controlling Graphene Corrugation on Lattice-Mismatched Substrates. *Phys. Rev. B* **2008**, *78*, 073401.
- (44) Haberer, D.; Vyalikh, D. V.; Taioli, S.; Dora, B.; Farjam, M.; Fink, J.; Marchenko, D.; Pichler, T.; Ziegler, K.; Simonucci, S.; et al. Tunable Band Gap in Hydrogenated Quasi-Free-Standing Graphene. *Nano Lett.* **2010**, *10*, 3360–3366.
- (45) Klues, M.; Hermann, K.; Witte, G. Analysis of the Near-Edge X-Ray-Absorption Fine-Structure of Anthracene: A Combined Theoretical and Experimental Study. *J. Chem. Phys.* **2014**, *140*, 014302.
- (46) Oji, H.; Mitsumoto, R.; Ito, E.; Ishii, H.; Ouchi, Y.; Seki, K.; Yokoyama, T.; Ohta, T.; Kosugi, N. Core Hole Effect in NEXAFS Spectroscopy of Polycyclic Aromatic Hydrocarbons: Benzene, Chrysene, Perylene, and Coronene. *J. Chem. Phys.* **1998**, *109*, 10409–10418.
- (47) Betti, M. G.; Kanjilal, A.; Mariani, C. Electronic States of a Single Layer of Pentacene: Standing-Up and Flat-Lying Configurations. *J. Phys. Chem. A* **2007**, *111*, 12454–12457.
- (48) Chioldi, M.; Gavioli, L.; Beccari, M.; Di Castro, V.; Cossaro, A.; Floreano, L.; Morgante, A.; Kanjilal, A.; Mariani, C.; Betti, M. G. Interaction Strength and Molecular Orientation of a Single Layer of Pentacene in Organic-Metal Interface and Organic-Organic Heterostructure. *Phys. Rev. B* **2008**, *77*, 115321.
- (49) Solomon, J.; Madix, R.; Stöhr, J. Orientation and Absolute Coverage of Benzene, Aniline, and Phenol on Ag (110) Determined by NEXAFS and XPS. *Surf. Sci.* **1991**, *255*, 12–30.
- (50) Hitchcock, A.; Fischer, P.; Gedanken, A.; Robin, M. Antibonding Sigma\* Valence MOs in the Inner-Shell and Outer-Shell Spectra of the Fluorobenzenes. *J. Phys. Chem.* **1987**, *91*, 531–540.
- (51) Fratesi, G.; Lanzilotto, V.; Floreano, L.; Brivio, G. P. Azimuthal Dichroism in Near-Edge X-ray Absorption Fine Structure Spectra of Planar Molecules. *J. Phys. Chem. C* **2013**, *117*, 6632–6638.
- (52) Alagia, M.; Baldacchini, C.; Betti, M. G.; Bussolotti, F.; Carravetta, V.; Ekström, U.; Mariani, C.; Stranges, S. Core-Shell Photoabsorption and Photoelectron Spectra of Gas-Phase Pentacene: Experiment and Theory. *J. Chem. Phys.* **2005**, *122*, 124305.
- (53) Bjork, J.; Stafstrom, S.; Hanke, F. Zipping Up: Cooperativity Drives the Synthesis of Graphene Nanoribbons. *J. Am. Chem. Soc.* **2011**, *133*, 14884–14887.
- (54) Blankenburg, S.; Cai, J.; Ruffieux, P.; Jaafar, R.; Passerone, D.; Feng, X.; Mullen, K.; Fasel, R.; Pignedoli, C. A. Intraribbon Heterojunction Formation in Ultrananow Graphene Nanoribbons. *ACS Nano* **2012**, *6*, 2020–2025.
- (55) Pacilé, D.; Papagno, M.; Rodríguez, A. F.; Grioni, M.; Papagno, L.; Girit, Ç.; Meyer, J.; Begtrup, G.; Zettl, A. Near-Edge X-ray Absorption Fine-Structure Investigation of Graphene. *Phys. Rev. Lett.* **2008**, *101*, 066806.
- (56) Beernink, G.; Gunia, M.; Dötz, F.; Öström, H.; Weiss, K.; Müllen, K.; Wöll, C. Synthesis of Polycyclic Aromatic Hydrocarbons and Graphite Islands via Surface-Induced Reaction of Small Molecules. *ChemPhysChem* **2001**, *2*, 317–320.